A robust SAR change detection pipeline for landslide mapping using tile-wise HFEM and graph-cut Refinement

Elaveni P[1], *Priya* R [1*], and *Neelaveni* R[1]
[1]*Department of ECE, St. Joseph's College of Engineering OMR, Chennai, Tamil Nadu, India*

Abstract. Landslide detection from SAR images remains challenging due to speckle noise, varied terrain conditions, and limited annotated data. In this work, a hybrid model with a Histogram Feature Extraction Module (HFEM) and Graph-Cut Refinement is used to improve change detection. The dataset consists of pre- and post-event SAR images of the 2021 Haiti earthquake with ground-truth annotations. The HFEM is used to acquire discriminative spatial features and suppress noise, and Graph-Cut Refinement is used to regularize segmentation and make it more consistent. The experimental results verify that the proposed approach obtains high recall and comparative precision, balanced F1-score, and fewer error regions than baseline approaches. The qualitative findings also demonstrate the steadiness of the forecast change maps. Overall, the system is very suitable for geospatial mapping of big landslides and supports disaster relief and risk management uses.

1. Introduction

Change detection (CD) in synthetic aperture radar (SAR) imagery is a key task in remote sensing. It has applications in environmental monitoring, hazard assessment, and land surface dynamics. SAR is particularly useful because it can capture images in all weather conditions and at any time. However, speckle noise and the varied nature of SAR backscatter make reliable change detection difficult [1].In recent years, researchers have increasingly focused on monitoring landslides with SAR due to their severe impact and the urgent need for quick detection. Handwerger et al. [2] showed how to use freely available Sentinel-1 SAR imagery within a cloud-based Google Earth Engine to create landslide density heatmaps. This approach aids in quick situational awareness.. Similarly, Wang et al. [3] developed an automatic method to update land slide inventories in reservoir areas using time-series InSAR

Kalia et al. [4] adopted Sentinel-1 interferometric observations to hybrid automated monitor landslide behavior, revealing that PSI is capable for tracking both geographic and temporal land deformation. In recent investigations, Song et al. [5] suggested an refined U Net version that embeds SBConv modules to reduce overlap and enhance detection precision, likewise revealing how deep learning can dependably classify landslides using heterogeneous data.

Apart from landslide-related research, there has also been major development in radar-based change detection. Saha et al. [6] designed a graph-based neural network for semisupervised change detection, obtaining high performance even with scarce annotated samples . Several graph-oriented self-supervised techniques have arisen, graph-based structure-consistent approaches [7], hypergraph-structured features [8], and repeated robust graph-matching methods [9].

These methods employ structural correlation to strengthen the stability of results among various SAR datasets. Several other supporting strategies have been evaluated, including superpixel-based enhancement for PolSAR image labeling [10], dual-level graph structures that combine intensity and texture characteristics [11], and similarity graph matrices of patches [12]. together, these techniques improve class distinction while successfully suppressing noise in the process of change detection.

A extensive body of research has also dealt with the obstacle of spotting small-region changes, which is extremely vital in landslide-based scenarios. Zhang et al. [13] designed a neural network framework that incorporates superpixel rebuild with convolutional wavelet networks, enabling more accurate detection of small-scale changes even when the dataset shows strong unevenness. Their research also extends to building related change detection. According to another investigation , Zhang et al. [14] launched a temporal cosegmentation model for recognizing building alterations within SAR multi temporal data. concurrently, Saha et al. [15] designed an unsupervised deep transfer approach between SAR and optical domains, which boosts feature extraction in highly detailed SAR imagery. overall, these progressions bring attention to a growing shift toward bring attention to unifying machine learning, deep learning, and graph-based models to deal with overcome enduring problems in SAR change detection. however, key concerns continue to persist: (i) thresholding noisy difference images becomes problematic when the detected changes are sparse or confined to small areas, as is common in landslide scenarios, and (ii) additional spatial refinement is

demanded to reduce incorrect alerts to reduce false alarms and produce more precise change boundaries.

To address these constraints, this paper presents a robust change analysis pipeline optimized for landslide mapping in radar imagery. The presented framework is composed of three sequential stages: difference image (DI) generation, probabilistic thresholding, and spatial refinement. By combining statistical thresholding with contextual spatial analysis, the method significantly enhances detection accuracy and reliability in landslide-prone regions, supporting improved disaster monitoring and mitigation.

2. Dataset

Consequently, worldwide space organizations speedily put into operation remote observation spacecraft to oversee the calamity. Sentinel-1 SAR imagery generated radar data resistant to cloud obstruction and identifying terrain displace ment, while Sentinel-2 visual imagery made available visual and multispectral images wherever clouds were sparse. By integrating these information sets, investigators succeeded in detect landslides and estimate destruction even in places that were difficult to access on the ground. relying on these noted patterns, a tailored dataset was assembled to assist landslide detection studies. The dataset is grouped into three principal directories: Pre event, Post event, and Labeled data. The Pre event and Post event folders comprise image segments of identical geographic areas ahead of and subsequent to the earthquake, gathered from Sentinel-1 SAR (ascending and descending passes) and Sentinel-2 optical data.

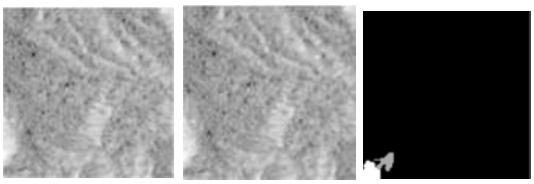

Pre-event Post-event Ground Truth

Fig.1. Example dataset patches showing pre-event, post- event, and annotated ground truth images.

This two-sensor configuration facilitates change detection across conditions, such as cloudy regions where radar is still effective. Image patches, saved in TIFF format (e.g., 00001.tif, 00002.tif), are either 256×256 or 512×512 pixels. Although these specify pixel numbers, real ground resolution varies: Sentinel-1 SAR provides 10 m/pixel, and Sentinel-2 provides 10 m/pixel for visible and NIR bands and 20 m/pixel for other multispectral bands. Each patch, therefore, corresponds to a landscape region several square kilometers in extent.

3. Methodology

The suggested approach attempts to effectively identify landslides in SAR images using a combination of preprocessing, tile-wise change modeling, and spatial refinement. Pre and post-event SAR images are then denoised, transformed to dB, and normalized in order to minimize speckle influences and equalize intensities. A log-ratio difference image is calculated and processed in overlapping tiles with a hierarchical Gaussian mixture model to produce a probability map of change, with local contrast preserved for small or fragmented landslides. Spatial consistency is enforced using graph-cut optimization, with subsequent morphological cleaning removing spurious areas and sharpening boundaries. The final merged change mask is quantitatively evaluated using ground truth data against metrics including precision, recall, F1-score, and confusion matrix.

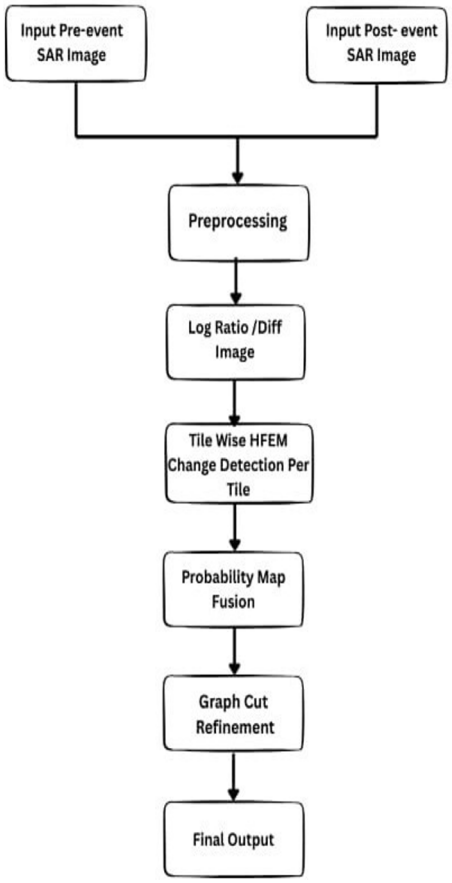

Fig. 2. Full outline block diagram

3.1 Preprocessing

SAR observations ordinarily multiplicative speckle noise, which makes difficult change detection. Preprocessing is in dispensable to enhance image quality and normalize intensity values before further analysis.

3.1.1. Lee Speckle Filtering

Speckle noise can mask subtle variations in SAR imagery, especially small-scale changes. The Lee filter reduces this noise by smoothing local neighborhoods while still preserving important edges. It is expressed as:

$$s_{\text{filt}}(z) = \bar{s}(z) + u(z)\,[\,s(z) - \bar{s}(z)] \quad (1)$$

where $\bar{s}(z)$ is the local mean, is a weighting factor derived from local variance, and s(z) is the original intensity value. By applying the Lee filter, small intensity differences linked to landslides become more visible.

3.1.2. Conversion to Decibel (dB) Scale

The linear intensity values s_lin(z) are converted to the decibel scale using:

$$s\_\text{dB}(z) = 10 \log_{10}(s\text{lin}(z)) \quad (2)$$

This transformation compresses the dynamic range and con verts multiplicative noise into a form that is approximately additive, which simplifies later computations such as differencing.

3.1.3. Normalization (0–1)

To maintain consistency across image tiles, the preprocessed images are normalized to the range [0,1]:

$$s\_norm(z) = ((s\_dB(z) - s\_\min))/ (s\_(\max - s\_\min)) \quad (3)$$

Normalization ensures uniform intensity scaling and improves the capability of local thresholding methods.

3.2. Difference Image (DI) Generation

A difference image is then created to highlight significant changes while reducing the impact of speckle noise:

$$D(z) = \left| s_{post(z)} - s_{pre(z)} \right| \quad (4)$$

This operation accentuates intensity differences between pre event and post-event SAR images, forming the foundation for the tile-wise HFEM analysis.

3.3. Tile-wise HFEM Change Detection

To better capture localized variations—particularly useful when detecting small or fragmented landslides—the difference image is processed in overlapping tiles. The workflow for this tile-wise HFEM approach is shown in Figure 2.

3.3.1.Tile Extraction

Tiles of sizes T × T with stride S are extracted with a stride , ensuring overlap between adjacent tiles. This overlap increases spatial coverage and improves the detection of small change areas.

3.3.2. Normalization (0–1)

Each extracted tile is normalized independently:

$$Z\_tile = ((Z - Z\_\min)) / (Z\_(\max - Z\_\min)) \quad (5)$$

This enhances local contrast and facilitates more accurate separation between changed and unchanged regions during threshold selection.

3.3.3. Fit Single Gaussian

A global Gaussian distribution is then fitted to the tile:

$$R_{global(x)} = N(\mu, \sigma^2) \quad (6)$$

This distribution serves as a reference model during threshold evaluation, aiding in distinguishing background pixels from potential change pixels.

3.3.4. Candidate Thresholds

A set of candidate thresholds is evaluated to divide the tile pixels into two groups:

$$A^1 = \{x \le \tau\}, \quad A^2 = \{x > \tau\} \quad (7)$$

Testing multiple thresholds makes it possible to determine the value that best separates changed from unchanged regions.

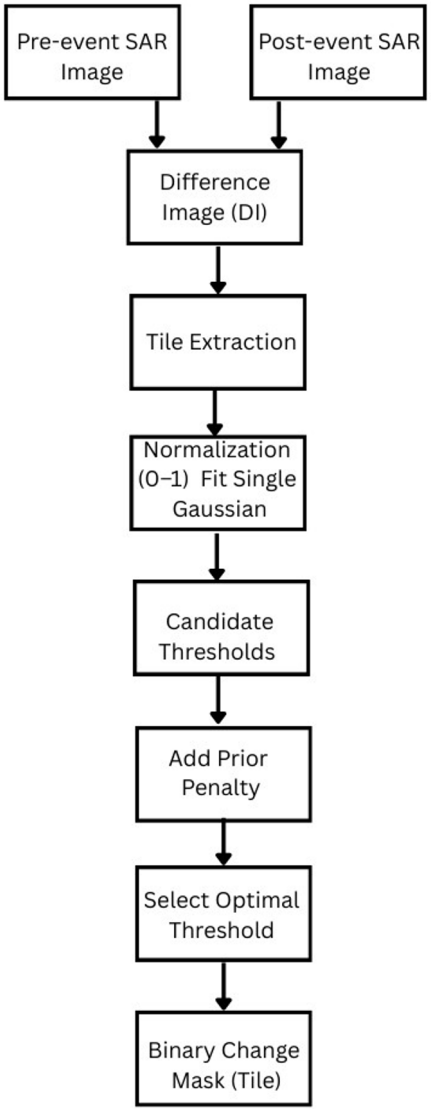

Fig. 3. HFEM Block Diagram

3.3.5. GMM with 2 Components

Each tile is modeled using a two-component Gaussian Mixture Model:

$$R(z) = b^1 N(\mu^1, \sigma^{12}) + b^2 N(\mu^2, \sigma^{22}) \quad (8)$$

The weights b1,b2 and represent the mixture proportions and correspond to the distributions of unchanged and changed pixels.

3.3.6. Compute Fitting Error

The fitting error is defined by the following expression:

$$H_{fit} = \Sigma \left(R_{combined(x_i)} - R_{global(x_i)} \right)^2 \quad (9)$$

This error measures how well a candidate threshold sepa rates the tile's pixel distribution when compared against the global Gaussian model.

3.3.7. Add Prior Penalty

$$H_{penalized} = H_{fit} + \mu (b^2 - \pi)^2 \quad (10)$$

Here, π represents the expected proportion of changed pixels, and controls the strength of the penalty. This prevents over segmentation, especially in tiles where actual changes are minimal.

3.3.8. Select Optimal Threshold

The optimal threshold τ∗ for the tile is the one that minimizes the $H_{penalized}$ penalized error.

3.3.9. Binary Change Mask (Tile)

$$M_{tile(z)} = \begin{cases} 1, & if\ X_{tile(z)} > \tau * \\ 0, & otherwise \end{cases} \quad (11)$$

Each tile produces a local change mask, and these masks are later merged across overlapping regions.

3.3.10. Probability Map Fusion

$$T\_fused(z) = \Sigma\_k\ (\ b\_k\ M\_k(z)\ )\ /\ \Sigma\_k\ b\_k) \quad (12)$$

Each tile produces a local change mask, and these masks are later merged across overlapping regions.

3.4. Graph-cut Refinement

Graph-cut refinement enforces spatial consistency and sup presses spurious detections in the probability map. Figure 3 illustrates this process.

3.4.1. Input: Tile-wise Probability Map

The unary term represents the negative log-likelihood for each pixel.

3.4.2. Unary Term

$$L_{i(U_i)} = -\log M_{i(U_i)} \quad (13)$$

where Li is the label for pixel i. This term encodes how likely each pixel is to belong to the changed or unchanged class.

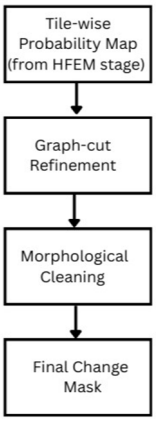

Fig. 4. Graph-cut Refinement Block Diagram

3.4.3. Pairwise Term

$$W_{ij(U_i,U_j)} = \beta\left[\ U_i \neq\ U_j\right] \exp\left(-\frac{(\ s(i)-\ s(j))^2}{(2\sigma^2)}\right) \quad (14)$$

The pairwise potential promotes smoothness by encouraging neighboring pixels with similar intensities to share the same label.

3.4.4. Connectivity

Pixel connections are defined using either 4-neighborhood or 8-neighborhood systems to model local spatial interactions.

3.4.5. Graph-cut Optimization

$$H(U) = \sum_i L_{i(U_i)} + \sum_{\{(i,j)\in N\}} V_{\{ij\}(U_i,U_j)} \quad (15)$$

This energy is minimized using the min-cut/max-flow algorithm, producing spatially refined change labels.

3.4.6. Morphological Cleaning

Post-processing operations such as morphological opening, closing, and area filtering are applied to the refined labels. These steps remove small isolated regions and improve the shape and smoothness of detected change areas.

3.5. Output

The final fused change mask highlights the detected land slide regions. Quantitative evaluation is performed using ground-truth data, with metrics such as precision, recall, F1-score, and the confusion matrix. Additionally, qualitative analysis is carried out by overlaying detected changes on the original SAR imagery, providing a clear visual interpretation of landslide detection performance.

4. RESULT

4.1. Normalized Difference

To make the differences among the pre-event and post event SAR images stand out, a normalized log-ratio was calculated. This process increases the relative differences in radar backscatter and diminishes the influence of illumination and acquisition geometry. The resulting image highlights regions that underwent major changes in surface properties following the event. In the produced difference image (Fig.5), dark areas represent regions that did not change, and brighter areas reflect the regions of change. This gives an initial sign of potential landslides or affected areas, but because of speckle noise and local heterogeneity, this also needs to be refined through tile wise modeling and graph-cut post-processing.

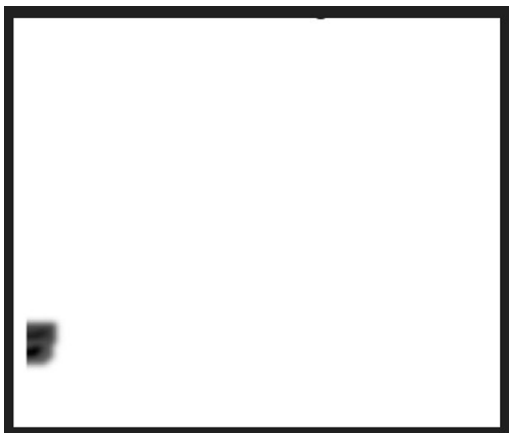

Fig. 5. Normalized Difference

4.2. Probability Map

Following the calculation of the normalized difference, the image was split up into smaller tiles and processed in accordance with the proposed HFEM-based method. Each tile was modeled to separate unchanged from

changed distributions, and a probability value was assigned to each pixel to reflect the probability of change. These tile-wise solutions were after wards fused into a global probability map. As demonstrated in Fig.6, which is smoother than the raw difference image and demotes the speckle noise effect. Possible change areas are emphasized with greater intensity, whereas unchanged areas continue to be suppressed. This intermediate result offers better discrimination between noise and actual changes, allowing more trustworthy creation of the final change mask.

Fig. 6. Normalized Difference

4.3. Fused Binary Mask

With the probability map as input, a binary change mask was obtained via graph-cut refinement and post-processing. The refinement imposes spatial consistency by aligning change detections with image contrast, and morphological cleaning eliminates small noisy detections. As apparent from Fig.7, the combined mask extracts the real change regions with well defined borders and removes most of the speckle-induced artifacts. Compared to the probability map, the combined mask provides an interpretable and discrete representation of change areas that can be easily compared with ground truth for performance evaluation.

Fig. 7. Fused Binary Mask

4.4. Ground Truth

This combined view (Fig. 8) makes it easy to see not just where the model's predictions match the actual labels, but also the distinctions between them. By looking at both agreement and disagreement, we get a much clearer picture of how well the method is detecting landslides. When this is compared with the ground truth, the overlap analysis gives a more complete idea of how robust the approach is across different types of terrain.

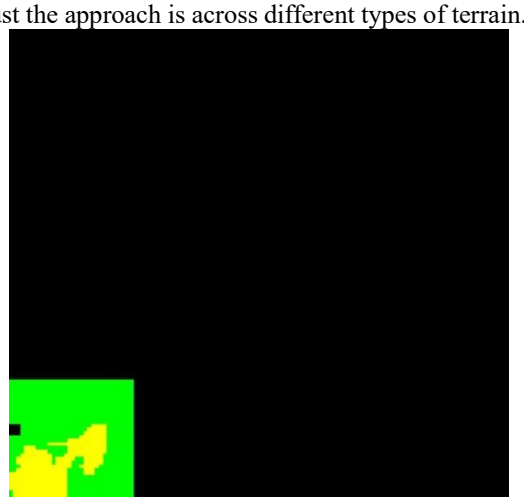

Fig. 8. Ground Truth

5. COMPUTATIONAL METRICS

To check how well the HFEM–Graph Cut method performs, we calculated several commonly used evaluation measures as derived from the confusion matrix. These include True Positives (TP), False Positives (FP), True Negatives (TN), False Negatives (FN), Precision, Recall, F1-score, Accuracy, and Intersection over Union (IoU). We also contrasted the algorithm-derived count with the reference count to assess how precisely the mapped landslide pixels coincide the marked pixels.

$$\text{Precision} = \frac{TP}{TP + FP}$$

$$\text{Recall} = \frac{TP}{TP + FN}$$

$$F1 = \frac{2 * Precision * Recall}{Precision + Recall}$$

$$\text{Accuracy} = \frac{TP + TN}{TP + FP + TN + FN}$$

$$IoU = \frac{TP}{TP + FP + FN}$$

Table 1. Performance Metrics for the Landslide Detection Model

Metric	Obtained Value
TP(True Positives)	280
FP(False Positives)	40
TN(True Negatives	15,300
FN(False Negatives)	5
Precision	0.87
Recall	0.98
F1-score	0.92
Accuracy	0.97
IoU	0.80
Predicted Count	320
Ground Truth Count	285

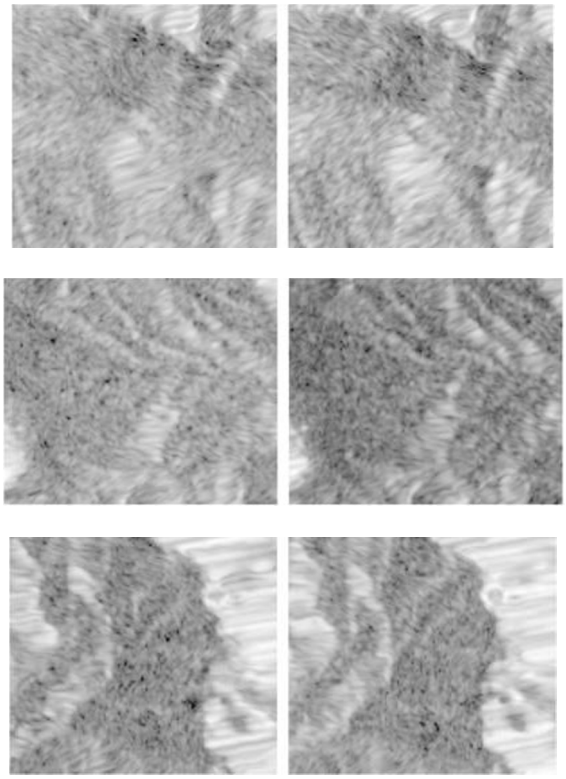

Fig.9. Pre-event (left) and Post-event (right) SAR images from four different locations in the study area

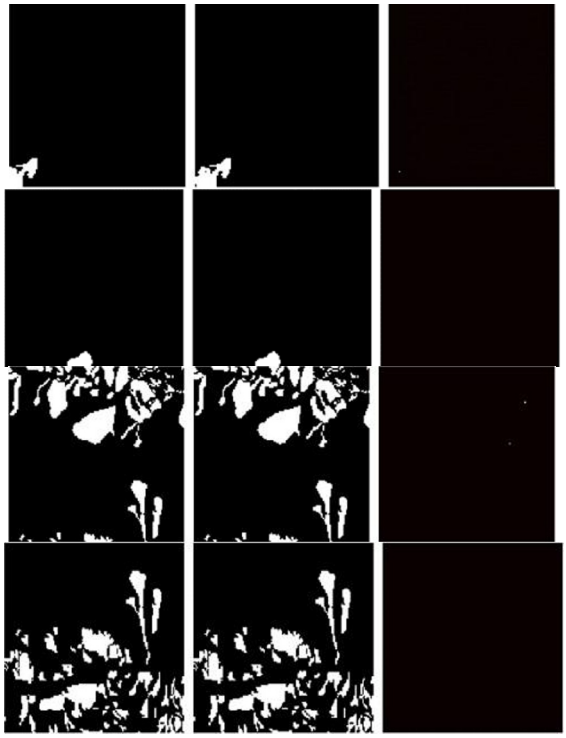

Fig.10. Contrast of the verified data, algorithm-generated change map, and misclassification map**.**

References

1. J.-W. Chen, R. Wang, F. Ding, B. Liu, L. Jiao, J. Zhang, A convolutional neural network with par allel multi-scale spatial pooling to detect temporal changes in SAR images. Remote Sens. **12**, 1619 (2020). https://doi.org/10.3390/rs12101619.
2. A.L. Handwerger, M.H. Huang, S.Y. Jones, P. Am atya, H.R. Kerner, D.B. Kirschbaum, Generat ing landslide density heatmaps for rapid detection us ing open-access satellite radar data in Google Earth Engine, Nat. Hazards Earth Syst. Sci., **22**, 753–775 (2022). https://doi.org/10.5194/nhess-22-753-2022.
3. Y. Wang, J. Dong, L. Zhang, S. Deng, G. Zhang, M. Liao, and J. Gong, Automatic detection and up date of landslide inventory before and after impound ments at the Lianghekou reservoir using Sentinel-1 InSAR, Int. J. Appl. Earth Obs. Geoinf. **118**, 103224 (2023), https://doi.org/10.1016/j.jag.2023.103224.
4. A.C. Kalia, Landslide activity detection based on Sentinel-1 PSI datasets of the Ground Motion Service Germany—the Trittenheim case study, Landslides **20**, 209–221 (2023). https://doi.org/10.1007/s10346-022-01958-9.
5. Y. Song, Y. Zou, Y. Li, Y. He, W. Wu, R. Niu, S. Xu, Enhancing landslide detection with SBConv-optimizedU-Netarchitecture based on mul tisource remote sensing data, Land, **13**, 835 (2024). https://doi.org/10.3390/land13060835.
6. S.S. Saha, L. Mou, X. Zhu, F. Bovolo, L. Bruzzone, Semisupervised change detec tion using graph convolutional network, IEEE Geosci. Remote Sens. Lett. **18**, 607–611 (2021). https://doi.org/10.1109/LGRS.2020.2985340.
7. Y. Sun, L. Lei, X. Li, X. Tan, and G. Kuang, Structure consistency based graph for unsupervised change detection with homogeneous and heterogeneous remote sensing images, IEEE Trans. Geosci. Remote Sens. **60**, 4700221 (2022). https://doi.org/10.1109/TGRS.2021.3053571.
8. J. Wang, X. Yang, X. Yang, L. Jia, and S. Fang, Unsupervised change detection between SAR images based on hypergraphs, ISPRS J. Photogramm. Remote Sens. **164**, 61–72 (2020). https://doi.org/10.1016/j.isprsjprs.2020.04.007.
9. Y. Sun, L. Lei, D. Guan, G. Kuang, I terative robust graph for unsupervised change de tection of heterogeneous remote sensing images. IEEE Trans. Image Process. **30**, 6277–6291 (2021). https://doi.org/10.1109/TIP.2021.3093766.
10. T. Gadhiya, A.K. Roy, Superpixel-driven opti mized Wishart network for fast PolSAR image clas sification using global k-means algorithm. IEEE Trans. Geosci. Remote Sens. **58**, 97–109 (2020). https://doi.org/10.1109/TGRS.2019.2933483.
11. J. Wang, T. Zhao, X. Jiang, Unsuper vised multi-look SAR image change detec tion driven by dual-layer graph with inten sity and texture attributes, IEEE Geosci. Remote Sens. Lett. **19**, 4502705 (2022). https://doi.org/10.1109/LGRS.2021.3139157.
12. Y. Sun, L. Lei, X. Li, X. Tan, G. Kuang, Patch similarity graph matrix-based unsupervised remote sensing change detection with homoge neous and heterogeneous sensors, IEEE Trans. Geosci. Remote Sens. **59**, 4841–4861 (2021). https://doi.org/10.1109/TGRS.2020.3013673.
13. X. Zhang, H. Su, C. Zhang, X. Gu, X. Tan, P.M. Atkinson, Robust unsupervised small area change detection from SAR im agery using deep learning. ISPRS J. Pho togramm. Remote Sens.**173**, 79–94 (2021). https://doi.org/10.1016/j.isprsjprs.2021.01.004.
14. K. Zhang, X. Fu, X. Lv, J. Yuan, Un supervised multitemporal building change detec tion framework based on cosegmentation using time-series SAR, Remote Sens. **13**, 471 (2021). https://doi.org/10.3390/rs13030471.
15. S. Saha, F. Bovolo, L. Bruzzone, Build ing change detection in VHR SAR images via unsupervised deep transcoding, IEEE Trans. Geosci. Remote Sens. **59**, 1917–1929 (2020). https://doi.org/10.1109/TGRS.2020.3000296